

## Article

# Characteristics of Natural Background Radiation in the Lubin Mine, Poland

Agata Walencik-Lata <sup>1,\*</sup>, Katarzyna Szkliniarz <sup>1</sup>, Jan Kisiel <sup>1</sup>, Kinga Polaczek-Grelik <sup>2</sup>, Karol Jędrzejczak <sup>3</sup>, Marcin Kasztelan <sup>3</sup>, Jacek Szabelski <sup>3</sup>, Jerzy Orzechowski <sup>3</sup>, Przemysław Tokarski <sup>3</sup>, Włodzimierz Marszał <sup>3</sup>, Marika Przybylak <sup>3</sup>, Lech Stolecki <sup>4</sup>, Tomasz Selerowicz <sup>4</sup> and Krzysztof Fuławka <sup>4</sup>

<sup>1</sup> August Chełkowski Institute of Physics, University of Silesia in Katowice, 75 Pułku Piechoty 1, 41-500 Chorzów, Poland

<sup>2</sup> NU-Med Cancer Diagnosis and Treatment Centre Katowice, Ceglana 35, 40-514 Katowice, Poland

<sup>3</sup> National Centre for Nuclear Research, 28 Pułku Strzelców Kaniowskich 69, 90-558 Łódź, Poland

<sup>4</sup> KGHM CUPRUM Research & Development Centre, Sikorskiego 2-8, 53-659 Wrocław, Poland

\* Correspondence: agata.walencik@us.edu.pl; Tel.: +48-32-3497739

**Abstract:** There has been growing interest in using underground locations for applications in various fields, including research. In Poland, for several years, attempts have been made to build an underground laboratory. For this purpose, selecting an appropriate location requires a detailed analysis of the level of natural radioactivity. The present study presents detailed characteristics of the natural background radiation in close vicinity to shaft L-VI of the Lubin mine, at the depth of 910 m (2275 m w.e.). The in situ measurement of the photon flux in the 7–3150 keV energy range was equal to  $8.08 \pm 0.90 \text{ cm}^{-2}\text{s}^{-1}$ , and the gamma-ray dose rate of  $0.070 \pm 0.010 \text{ } \mu\text{Sv/h}$  with the highest contribution from  $^{40}\text{K}$  and  $^{214}\text{B}$  isotopes. The thermal neutron flux measured using helium counters was equal to  $4.2 \pm 0.9 \times 10^{-6} \text{ cm}^{-2}\text{s}^{-1}$ . The radon concentration in the air measured with the RAD7 monitor showed low values ranging from 0 to  $15.3 \text{ Bq/m}^3$ . Laboratory measurements of rocks using alpha and gamma spectrometry techniques showed a significant variation in the concentration of  $^{226}\text{Ra}$  and  $^{234,238}\text{U}$  isotopes, and the highest concentration values were recorded for shales. The  $^{40}\text{K}$ ,  $^{234,238}\text{U}$  and  $^{226}\text{Ra}$  isotopes make the greatest contribution to the natural radioactivity of analyzed rocks.

**Keywords:** natural radiation; underground research laboratory; radioisotopes concentration



**Citation:** Walencik-Lata, A.; Szkliniarz, K.; Kisiel, J.; Polaczek-Grelik, K.; Jędrzejczak, K.; Kasztelan, M.; Szabelski, J.; Orzechowski, J.; Tokarski, P.; Marszał, W.; et al. Characteristics of Natural Background Radiation in the Lubin Mine, Poland. *Energies* **2022**, *15*, 8478. <https://doi.org/10.3390/en15228478>

Academic Editors: Jesús Polo, David C. Sassani, Russell Chris Camphouse and Geoff Freeze

Received: 17 October 2022

Accepted: 9 November 2022

Published: 13 November 2022

**Publisher's Note:** MDPI stays neutral with regard to jurisdictional claims in published maps and institutional affiliations.



**Copyright:** © 2022 by the authors. Licensee MDPI, Basel, Switzerland. This article is an open access article distributed under the terms and conditions of the Creative Commons Attribution (CC BY) license (<https://creativecommons.org/licenses/by/4.0/>).

## 1. Introduction

There are several dozen operating underground laboratories (ULs) worldwide, with various applications. They conduct basic research in particle physics, astrophysics, and nuclear physics but also perform technical and biomedical measurements that require a low background from cosmic rays and natural radioactivity. Such conditions are impossible to obtain on the surface of the Earth. Therefore, deep underground environmental conditions create new, unique opportunities for various types of research and measurements, interdisciplinary. There are also underground laboratories that deal with the final disposal of spent nuclear fuel. One of them is Äspö Hard Rock Laboratory, located in Sweden. They investigate, inter alia, the interaction of bentonite and copper canisters with rock under realistic conditions, as well as determine the role of the rock as a barrier [1]. In Europe, the leading laboratories are Gran Sasso, located in Italy, Modane in France, Canfranc in Spain and Boulby in Great Britain.

There is currently no operating underground laboratory in Poland, although efforts to create it began in 2010. At that time, the Polkowice-Sieroszowice mine, owned by KGHM Polska Miedź S.A., was one of the candidates for an underground laboratory to participate in the European project LAGUNA FP7 with a liquid argon detector for physics research [2–4]. The natural radioactivity measurements carried out at that time in the salt

layer showed an extremely low level of natural radioactivity (lower than in the leading European underground laboratories). However, the idea was rejected at the time due to the strictly mining policy of KGHM's mines. Currently, intensive work is being carried out in Poland to find a suitable location to create an underground research laboratory characterized by a low level of natural radioactivity. Several scientific and state institutions are involved in this work. One of the considered locations is the Lubin mine, the oldest KGHM Mining Division in the Lower Silesian Copper Basin (LSCB). A large part of the mine workings is out of use, but chosen workings are still maintained for ventilation and transport reasons. The construction of an underground laboratory in these locations could give these parts of the mine a second 'life' and better utilization. For this purpose, preliminary measurements of natural background radiation were required to determine if the underground workings of the Lubin mine are suitable for performing chosen non-mining activities. Therefore, a detailed analysis of natural radioactivity was carried out in close vicinity to shaft L-VI of the Lubin mine, at a depth of 910 m (about 2275 m w.e.).

Radionuclides are widespread in the environment in various concentrations. Natural radioactivity can be divided into three groups: long-lived radionuclides, radionuclides present in decay chains, and cosmogenic radionuclides. Most naturally occurring radioactive elements are grouped into three decay chains, and  $^{232}\text{Th}$ ,  $^{238}\text{U}$ , and  $^{235}\text{U}$  isotopes are the protoplasts of the natural radioactive series. However, due to the time of half-life, the  $^{238}\text{U}$  and  $^{232}\text{Th}$  decay series are of major importance. Cosmic radiation is not only a source of ionizing radiation but also produces many radioactive elements in the atmosphere and on the Earth. Cosmogenic isotopes are formed as a result of the reaction of high-energy particles with the components of the atmosphere (nitrogen, oxygen, and argon) and the dust particles present in it and with the surface layers of the lithosphere [5]. From the point of view of irradiation of living organisms, the most important are:  $^3\text{H}$ ,  $^7\text{Be}$ ,  $^{14}\text{C}$  and  $^{22}\text{Na}$ . Elements belonging to the radioactive series of  $^{238}\text{U}$  uranium, thorium and  $^{40}\text{K}$  isotope are the primary sources of natural ionizing radiation

The aim of the present study was to provide detailed characteristics of the natural radioactivity of the studied location. The research includes in situ measurements with the use of gamma spectrometry, the radon concentration in the air, and thermal neutron flux measurements. The laboratory alpha spectrometry measurements of  $^{234,238}\text{U}$  concentrations in rock and water samples collected in the shaft were performed. Moreover, radium  $^{226,228}\text{Ra}$  and potassium  $^{40}\text{K}$  concentrations in rock samples were determined using the gamma spectrometry technique. Based on estimated concentrations of  $^{226,228}\text{Ra}$  and potassium  $^{40}\text{K}$  in analyzed rock samples, potential radiological risk indices have been calculated.

### 1.1. Description of Deposit

Permian deposits from the described area were deposited in the SE part of the South Permian Basin, the so-called Polish Permian Basin. The basin, developed due to rifting between Late Carboniferous and Early Permian, extends from Great Britain to Poland. It was filled with Lower and Upper Rotliegend strata deposited mostly as clastic and volcanic (in the lower part) rocks [6]. In the top part of the strata, the presence of paleo-dunes has been confirmed [7–9]. Those paleomorphological undulations were an important factor influencing the lateral and vertical distribution of younger sediments [7,10]. In the Zechstein times (Late Permian), transgression of the waters from the Boreal Ocean flooded the area of intracontinental depression [11,12]. That resulted in the remobilization of the aeolian sand. The oversaturated sand displacement, from tops to depressions between dunes, reduced the elevations inherited from the previous landscape. In the topmost parts of the white sandstones, sedimentological structures and fauna clearly indicate underwater deposition [13]. The detrital materials of the white sandstones (Weissliegend) are mainly grains of quartz and, less often, feldspars, micas, and igneous and metamorphic rocks fragments [14]. Cements are mainly composed of illite, carbonates, sulfides, and quartz (less often), close to the top of sandstone elevations sulfates [14]. During the next phase, nearshore, calcareous deposits were settled (now several dozen centimeters-thick so-called

“basal limestone”). On the regional scale, in the depressions between paleodunes, fine grained muds were deposited. At the same time, on the topmost parts of paleoelevations, small or no deposition of mud took place. That resulted in the elongated (NNW-SSE) areas without Coppershale (Figure 1). Coppershale thickness varies from 0 to 1.7 m [15]. Shales are composed of illite, glauconite, carbonates, quartz, and phengite. Phosphates and feldspars were also identified [14]. During the deposition of the mud, below the wave base, the euxinia existed, which made possible the preservation of up to 40 wt.% of organic matter [16]. Subsequently, muds were gradually replaced by carbonate deposition of Zechstein limestones. The Zechstein Limestones (Ca1) are composed of carbonates with varying dolomite–calcite content. With an upward increase in the volume of carbonates, a decrease in the content of organic matter is observed. In the area of copper mines, three characteristic carbonate facies can be distinguished regionally: carbonate platform, slope and basin (Figure 1). On the platform, more than 100 m of carbonates thickness was revealed; then, on the slope, thickness gradually dropped and reached a few meters in the basinal part.

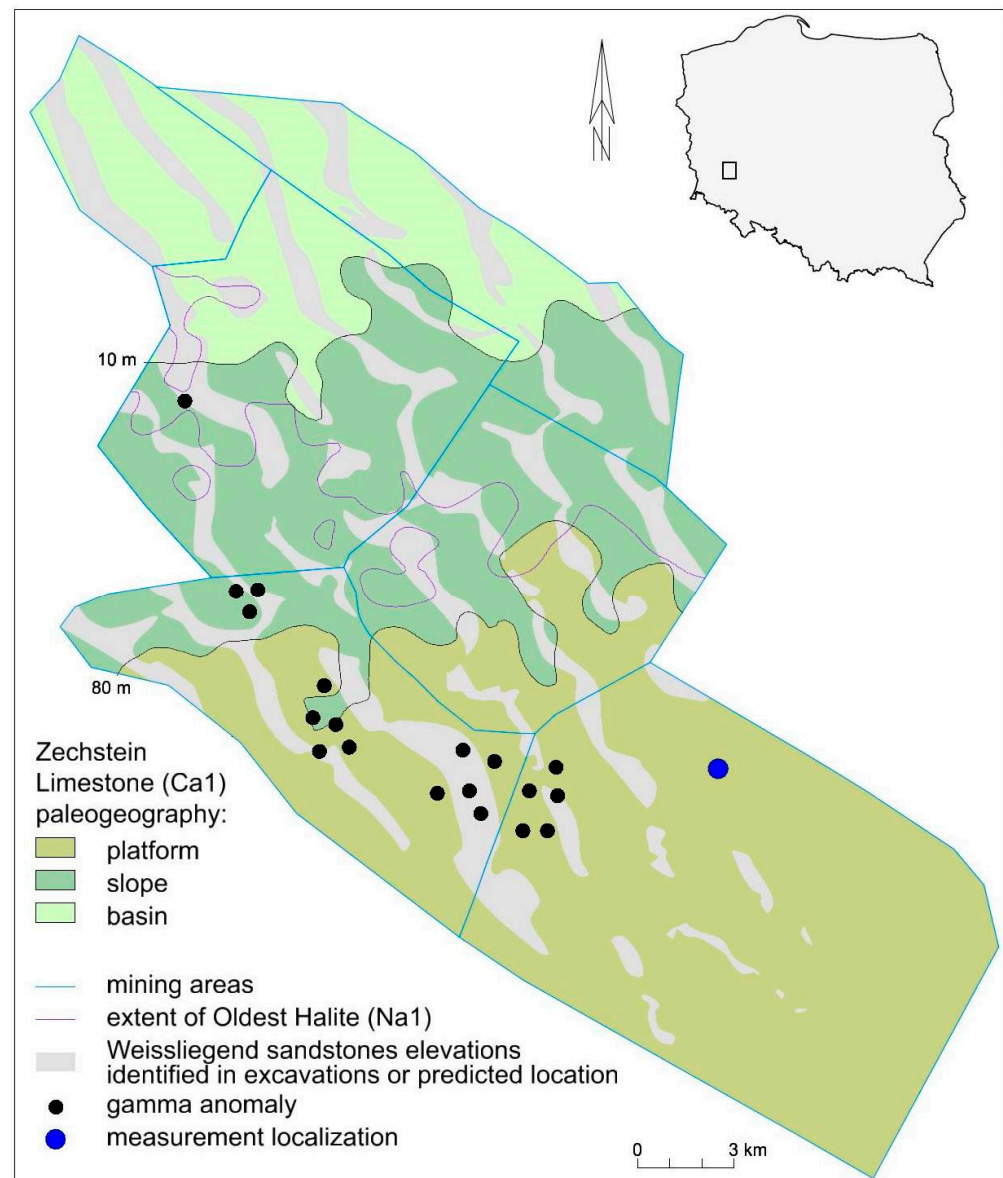


**Figure 1.** Measurement site on a geological background. Gamma anomalies were marked based on [17].

The main mineralized, and thus mined, lithologies in the KGHM Polska Miedź S.A. mines are described above the lowest part of the Zechstein sediments: white sandstones, shales, and dolomites. On the carbonates, anhydrite layers interbedded with salt were deposited. The Lower Anhydrite (A1a) thickness changes from a few meters to more than 100 m and can vary significantly over short distances. A good negative correlation between the Lower Anhydrite thickness and the Oldest Halite can be observed. The thickness of salts varies from 0 to more than 180 m. Salt layers do not completely cover the mining areas. The present extent of salt layers crosscut the mining area approx. from E to W, and north to the Zechstein Limestone platform facies (Figure 1). Upper anhydrite (A1b), when the salt layer is absent, can be distinguished from Lower Anhydrite thanks to the anhydrite breccia layer (Br1). Upper anhydrite has an average thickness of around 50 m and closes the first evaporite cyclothem–Werra (PZ1).

The periodically isolated Zechstein Sea and dry climate conditions resulted, in the described area, in the development of three classical evaporitic deposition cycles: PZ1–Werra, PZ2–Stassfurt, and PZ3–Leine. The youngest period with more continental influence was deposited under more humid conditions (PZ4–Aller) [18]. Zechstein sediments were covered with thick Mesozoic and Cenozoic deposits.

In general, Permian and Mesozoic sediments are slightly tilted to the NE and NNE. The homocline was formed at the turn of the Mesozoic and Cenozoic. Therefore, especially southern parts of the copper mines, close to the Fore-Sudetic Block, are characterized by dense faulting. Structures created by older tectonic events were also recognized [19,20].

### 1.2. Site Geology

The Lubin mine is located in the Lower Silesia voivodeship north of the borders of Lubin city. The deposit's industrial resources amount to over 328 million tonnes of copper ore. The copper content in the ore is 1.28% on average, and the silver content is 54.5 g/Mg. The dominant lithological type of copper ore is sandstone, which accounts for nearly 70% of the resources. The depth of copper ore in the Lubin deposit ranges from 368 to 1006 m. The deposit is relatively shallow, just below loose Cenozoic sediments. In regions where discontinuities such as faults occur, exploitation is very difficult and sometimes simply impossible. The height of workings in the Lubin mine is characterized by variability in the range from 1.5 m up to 5.5 m. The average height of the workings is about 2.8 m. Within the mining level, three types of rocks occur. In the central part of the excavation level, Coppershales are present. These shales are bitumen-carbonate shales containing minerals of copper and other metals, e.g., silver, lead, nickel, cobalt and others. Above the Coppershales, there is a thick layer of carbonate rocks, mainly in the form of dolomites. These rocks are characterized by high strength. In turn, below the Coppershales strata, a thick layer of sandstone is located. The stratigraphic profile within the analyzed area is presented in Figure 2.

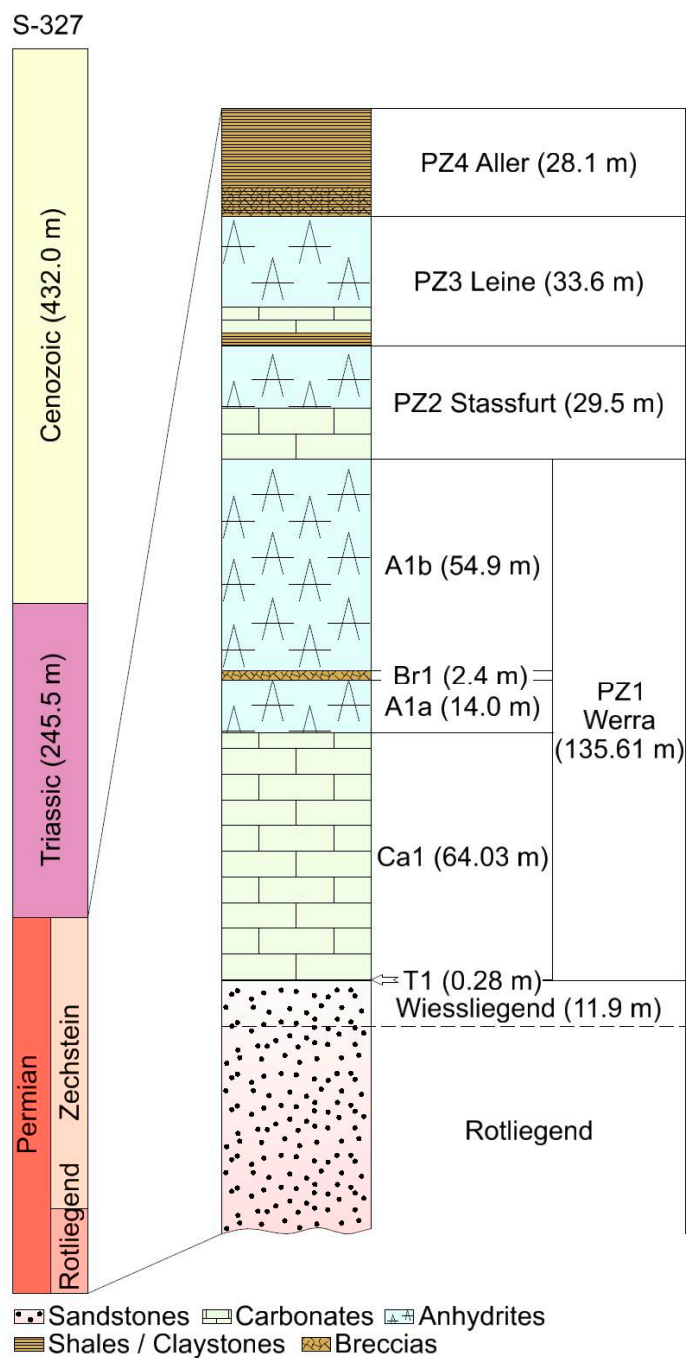


**Figure 2.** Geostatigraphic profile in the S-327 borehole (T1–Coppershale; Ca1–Zechstein Limestone; A1a–Lower Anhydrite; Br1–Anhydrite Breccia; A1b–Upper Anhydrite).

## 2. Materials and Methods

Measurements of the natural radioactivity were carried out at a distance of about 400 m from the L-VI ventilation shaft, at a depth of 910 m (2275 m w.e.) at the level of copper ore deposit excavation. The location of the measuring site, dimensions of the underground excavation and parameters of air in the area of measurements are presented in Figure 3. All measurements were performed with the same equipment and similarly as was done at the Polkowice-Sieroszowice mine in the anhydrite layer and at the GIG Experimental Mine ‘Barbara’ in sandstone rocks and described in detail in previous works [21,22]. The detectors were installed side by side (Figure 4) in the excavation near the Rdg-3/Rd-17.2 switching station chamber.

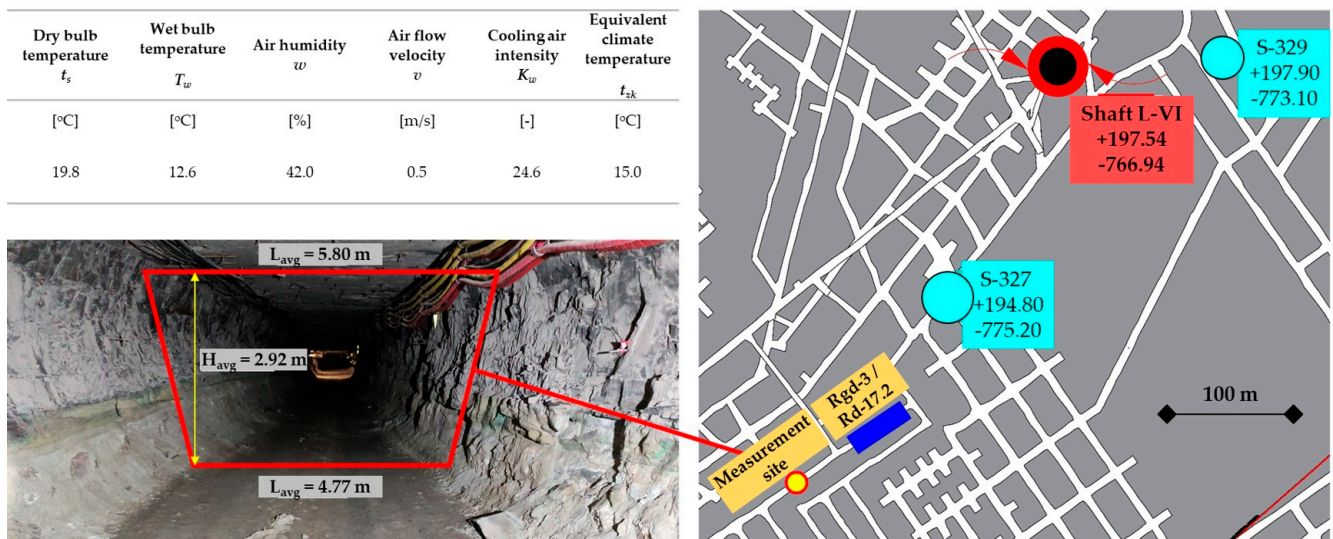


**Figure 3.** Geometry of underground excavation and air flow parameters in the area of the measuring site (left) and location of the ventilation shaft and exploration drills next to the area of the radiation measurement (right).

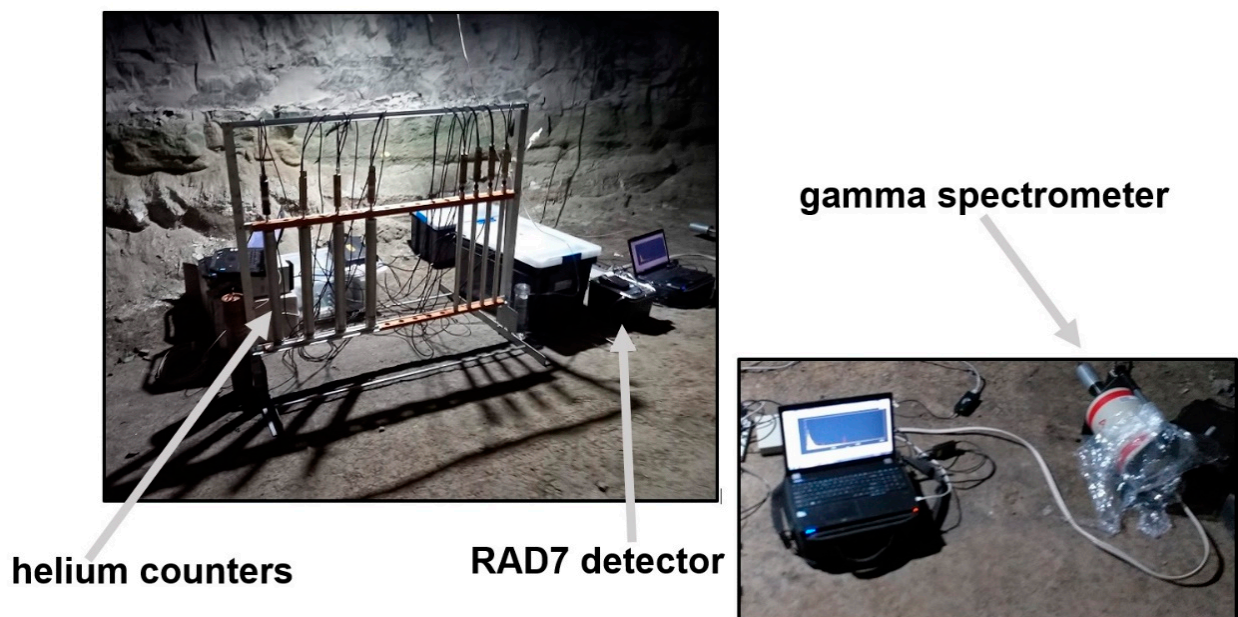


**Figure 4.** Measurement setup used during the measurements: helium counters; radon monitor RAD7 and HPGe spectrometer.

The height of the chamber was 2.92 m, while the width was 5.80 m, and at the bottom it was 4.77 m. In situ gamma radiation measurements were carried out using a semiconductor portable gamma spectrometer with the high purity germanium detector (HPGe); radon concentration measurements in the air using the RAD7 radon monitor; and the neutron flux was measured with helium counters. To carry out laboratory analysis (at the A. Chełkowski Institute of Physics, the University of Silesia in Katowice, Poland), six rock samples and one water sample were collected from the site where the in situ measurements were taken. The rock samples for laboratory analysis consisted of two samples of sandstone, dolomite, and shale. The concentration of uranium  $^{234,238}\text{U}$  radioisotopes in rock and water samples was measured by alpha spectrometry, while the content of radium  $^{226,228}\text{Ra}$  and potassium  $^{40}\text{K}$  in rock samples by gamma spectrometry technique.

### 2.1. In Situ Gamma Spectrometry

In situ gamma radiation measurements were made using a portable gamma spectrometer with the HPGe detector placed directly on the “floor”, with the window facing the closest wall about 80 cm away (Figure 4). The entire measuring equipment consisted of the portable spectrometer equipped with an HPGe coaxial detector (model: GR4020), In Spector™ 2000 multichannel analyzer (for data collection) and Genie™ 2000 v.3.2.1 software package (for spectra analysis). The Ge crystal has a mass of about 0.98 kg and a diameter equal to 61 mm. The HPGe detector has a relative efficiency of 40% and is equipped with a 0.6 mm-thick carbon window; the FWHM is 2.1 keV for the 1.33 MeV <sup>60</sup>Co line, and the peak-to-Compton ratio (P-to-C) is 57/1. The spectrometer is cooled with liquid nitrogen. The measuring range of the gamma radiation spectra was 7–3150 keV with a gain of 5. Before in situ measurements, energy and efficiency calibration of the detector was performed. Energy calibration was performed using the following sources: <sup>133</sup>Ba, <sup>137</sup>Cs, <sup>54</sup>Mn, <sup>57</sup>Co, <sup>109</sup>Cd, <sup>22</sup>Na, and <sup>60</sup>Co, having a diameter of 1 cm and about 10 kBq activity. The efficiency calibration was performed using ISOCS™ software (Canberra Industries, Inc., Meriden, CT, USA). A *room/box geometry with internal surface contamination* was used. It was modeled in Geometry Composer software (Canberra Industries, Inc.) in the energy range and 10–7000 keV for mono-energy photons. The uncertainty of the photon detection efficiency ranged from 4 to 15%. The software modeled that the radioactivity was distributed evenly between the four walls, while the radioactivity from the two far ends was assumed not to contribute to the measurement. The equation of detection efficiency based on photopeak net counts as a function of gamma radiation energy [keV] is described using a fifth-order polynomial as follows:

$$\ln(\epsilon) = -10.88 - 8.884\ln(E) + 5.996\ln(E)^2 - 1.428\ln(E)^3 + 0.1452\ln(E)^4 - 0.005426\ln(E)^5. \quad (1)$$

In the recorded gamma-ray spectrum, radioisotopes were identified based on the energy of the photopeaks. In Genie™ 2000 v.3.2.1 software, the areas under consecutive peaks were determined automatically by an analysis sequence, including an unidentified second difference fit and a nonlinear least-squares fit (LSQ).

Based on the gamma-ray spectra, the gamma-ray flux density, the effective dose rate and the total number of counts per second (cps) were calculated. The effective dose rate at the site of in situ measurements was determined using the photon flux to dose conversion factors taken from the ICRP report [23]. The photon flux determination method, effective dose rate and uncertainty estimation were described in our previous work [21].

### 2.2. In Situ Radon Measurement in Air

The concentration of <sup>222</sup>Rn in the air was measured using a RAD7 portable detector (DurrIDGE Company, Inc., Billerica, MA, USA). The detector was placed next to a gamma spectrometer and helium counters (Figure 4). This detector has several preprogrammed setups which can be applied to obtain <sup>222</sup>Rn concentration in the air. The monitor uses a semiconductor detector (Planar Silicon detector with a passivated ion) to generate an electrical signal from the alpha radiation and, through spectral analysis, differentiate alpha particles based on their energy. Moreover, the RAD7 monitor allows for radon concentration measurement in the air below 4 Bq/m<sup>3</sup> due to the low intrinsic background of the device lower than 0.2 Bq/m<sup>3</sup>. The measurements were performed using a 2-day protocol with a 1 h measurement cycle. First, in Sniff mode, radon concentration is calculated based on the daughter isotope of <sup>218</sup>Po. After three hours, for higher precision, the Sniff mode changes automatically to the Normal mode. In this mode, radon concentration is measured based on the signals originating from <sup>214</sup>Po and <sup>218</sup>Po isotopes.

### 2.3. $\alpha$ and $\gamma$ Laboratory Spectrometry Techniques

One water sample was collected in a 1.5 L polyethylene bottle and transferred to the laboratory for <sup>234,238</sup>U analysis using the alpha spectrometry technique. The sample was acidified with nitric acid to avoid the precipitation of iron on the wall of the bottle. Then,

the known amount of the  $^{232}\text{U}$  tracer was added to the sample. The chemical analysis was based on the procedure worked by Suomela [24]. Uranium was separated from the other alpha radionuclides on the anion exchange resin Dowex<sup>®</sup> 1  $\times$  8 ((Cl) type, 200–400 mesh). Uranium fraction was coprecipitated with  $\text{NdF}_3$  [25] and then filtered using a polypropylene filter (Pall Corporation, New York, NY, USA). A blank sample was prepared using 0.5 L of distilled water. Minimum Detectable Activity (MDA) equaled 0.5 mBq/L for both  $^{234,238}\text{U}$  isotopes and two days of blank sample measurement time. The measurements were performed with the use of alpha spectrometers 7401VR and Alpha Analyst<sup>™</sup> (Mirion Technologies (Canberra), Inc., Meriden, CT, USA) with semiconductor detectors (passivated implanted planar silicon (PIPS) detectors).

Six samples (two samples of dolomite, sandstone and shale) were taken at the site where in situ measurements were carried out. In the laboratory, samples were dried, ground and homogenized. The samples were placed in Marinelli containers, sealed to avoid radon leakage, and left for a month to achieve secular equilibrium between  $^{226}\text{Ra}$ ,  $^{228}\text{Ra}$  and their daughters in the uranium and thorium series. The activities of  $^{226,228}\text{Ra}$  and  $^{40}\text{K}$  concentrations were calculated using a standard prepared from certificated materials obtained from Central Laboratory for Radiological Protection in Poland. The activity concentration of the  $^{40}\text{K}$  isotope was calculated based on a 1460.8 keV photopeak. The concentrations of  $^{226}\text{Ra}$  and  $^{228}\text{Ra}$  isotopes were calculated as the weighted mean of the activities of daughter isotopes  $^{214}\text{Pb}$  (295.2, 351.9 keV),  $^{214}\text{Bi}$  (609.3, 1120.3 keV) and  $^{228}\text{Ac}$  (338.3, 911.1 keV), respectively. The laboratory measurements were performed using a gamma spectrometer from Canberra-Packard. The spectrometer consists of an HPGe coaxial detector (type: GC2018) of 60.7 mm crystal diameter, a mass of about 0.52 kg with a relative efficiency of 20% and Cryo-Pulse 5 Plus—an electrically powered cryostat. The detector was connected to a Digital Signal Analyser (DSA-LX). To reduce the external radiation background, the detector was placed in a low-background lead–copper shield manufactured by Ortec. The data acquisition and analysis was performed using Genie<sup>™</sup> 2000 v.3.4.1 software from Canberra-Packard. The detector had the P-to-C equal to 53.8/1 and an energy resolution (FWHM) of 1.7 keV for a 1.33 MeV gamma line from  $^{60}\text{Co}$ .

The sub-samples of about 1 g were prepared for the alpha-spectrometric measurements of  $^{234,238}\text{U}$  isotopes. Samples were transferred to PTFE pressure decomposition vessels and digested using a microwave unit MAGNUM II (ERTEC-Poland). At the beginning of the chemical preparation known activity of  $^{232}\text{U}$  was added to each sample. Wet mineralization of analyzed rocks was performed with the use of the following hot acids: HF,  $\text{HNO}_3$ , HCl with  $\text{H}_3\text{BO}_3$ . Then, uranium was pre-concentrated with iron and co-precipitated using ammonia at pH 9. The precipitate, dissolved in 8 M HCl, was passed through an ion-exchange column. The next steps of the chemical preparation were the same as those applied to the water sample. Details on the chemical analysis of samples and determination of the analyzed isotopes can be found in previous publications [22,26,27].

#### 2.4. Neutron Flux Measurements

To measure the thermal neutron flux, the same apparatus and the same method were used as in our earlier measurements at the Polkowice-Sieroszowice and GIG Experimental ‘Barbara’ mines [22]. It consists of measuring the counting rate using a setup of helium counters (sensitive to thermal neutrons), and then comparing the result with a simulation in which the setup was illuminated with an isotropic flux of thermal neutrons. The comparison of the measurement and simulation results allows for determining the real neutron flux at the measurement site. The assumption in the Monte Carlo simulation of an isotropic flux is a simplification, which, however, seems reasonable when a single measurement is made in the center of the mine tunnel.

The measurement setup consisted of helium counters (Figure 4), i.e., proportional gas counters filled with helium-3. The helium-3 nucleus captures a neutron invisible normally to the counter and then decays into two charged products: proton and tritium, which the counter can register. In this process, 764 keV of energy is released, which means that

in the spectrum of amplitudes of the recorded events, neutron events create an easily identifiable peak.

We used two types of counters: Centronic 50He3/190/50MS and ZDAJ NEM425A50. Both types had the classic form of 50 cm steel pipes, but differed in diameter: 5 cm for Centronic and 2.5 cm for ZDAJ. Four counters of each type were used in the measuring setup. All the counters were placed vertically in the form of a flat tray: first, 4 Centronic counters, then 30 cm break, then 4 ZDAJ counters; additionally, there were 5 cm intervals between the counters (Figure 4), which reduces the mutual shading effect.

When there was a trigger (exceeding the comparison threshold), the oscilloscope-like waveform was recorded for each counter, sampled with a frequency of 10 MHz and ADC dynamics of 10 bits. The length of the waveform was dynamically adjusted to the length of the appearing signal, but for correct neutron events, the length was 128 or 192 samples. The oscilloscope-like waveform allowed off-line analysis to distinguish neutron events from various disturbances by means of the pulse shape analysis. In view of the low counting rate (several counts per hour) and difficult mining conditions, shape analysis is critical for the precision of the measurement.

Finally, the recorded counting rate was compared with Monte Carlo simulations carried out using the Geant4 package [28] version 10.07 using the physical package QGSP\_BERT\_HP and NeutronHPThermalScattering, which is important for low energy neutron interactions with nucleons bound in nuclei. The comparison of the measurement and simulation results made it possible to determine the neutron flux at the measurement site.

### 3. Results and Discussion

#### 3.1. Analysis of the Gamma-Ray Spectrum

Figure 5 shows a 48 h gamma-ray spectrum recorded in shaft L-VI of the Lubin mine at a depth of 910 m. The total counting rate, similar to our previous works [21,22], was normalized to the day (d), energy (keV), and mass of the germanium crystal (kg). The total count rate per second in the energy range from 7 to 3150 keV is  $224.59 \pm 0.05$ . This result obtained in the Lubin mine is about 4 to 8 times higher than in the three main underground European laboratories (Modane, Boulby and Gran Sasso) [29–31], and 40 to 100 times higher than in the salt chamber in the Polkowice-Sieroszowice mine [32], but comparable to the anhydrite layer in the same mine [21].

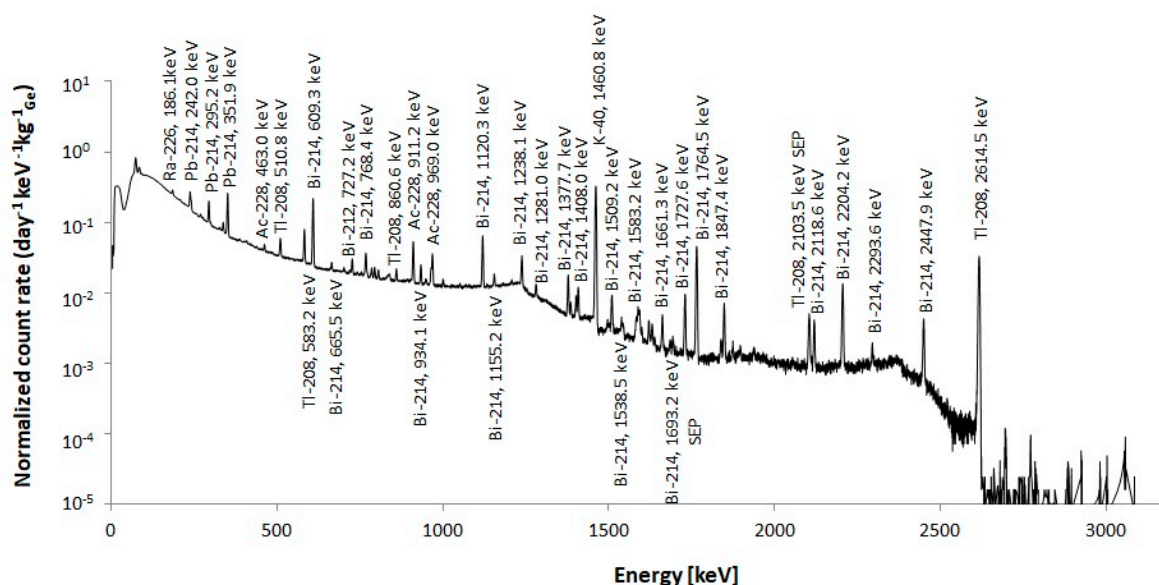


**Figure 5.** Gamma-ray spectrum registered at shaft L-VI and normalized to the day, photon energy, and germanium crystal mass. The main visible peaks are identified. Many low-energy lines between 20 and 150 keV were recognized, but for clarity of this presentation, they are not marked here.

Table 1 presents the apparent activity and effective dose rate estimated based on the registered in situ gamma-ray spectrum. The calculated gamma-ray flux and the effective dose rate based on the 48 h measurement of gamma-ray is  $8.08 \pm 0.90 \text{ cm}^{-2}\text{s}^{-1}$  and  $0.070 \pm 0.010 \text{ }\mu\text{Sv/h}$  ( $19.5 \pm 2.8 \text{ pSv/s}$ ), respectively. The largest contribution to the effective dose rate came from  $^{40}\text{K}$  (39.64%),  $^{214}\text{Bi}$  (34.23%) from the uranium series, and  $^{208}\text{Tl}$  (14.59%) from the thorium series. The gamma-ray flux is approximately 13 times greater than in the Polkowice-Sieroszowice mine in the anhydrite layer [21] at a depth of 1014.4 m and approximately 65 times higher than in the salt chamber at a similar depth (930 m) [33]. On the other hand, the effective dose rate is about 9 times higher than in the anhydrite layer and 39 times higher than in the salt chamber.

**Table 1.** Apparent activity in [ $\text{Bq}/\text{cm}^2$ ], effective dose rate (EDR) in [ $\text{pSv/s}$ ], with the calculated contribution (%) of each isotope to EDR estimated based on registered in situ gamma-ray spectrum. Uncertainties (denoted as  $\Delta$ ) are also presented.

Decay Chain	Nuclide	A <sub>apparent</sub> [ $\text{Bq}/\text{cm}^2$ ]	$\Delta$ [ $\text{Bq}/\text{cm}^2$ ]	EDR [ $\text{pSv/s}$ ]	$\Delta$ [ $\text{pSv/s}$ ]	% to EDR
Uranium	$^{234}\text{Th}$	0.24	0.05	0.004	0.001	0.02
	$^{234\text{m}}\text{Pa}$	1.62	0.36	0.042	0.007	0.22
	$^{226}\text{Ra}$	1.04	0.28	0.020	0.003	0.10
	$^{214}\text{Bi}$	1.60	0.29	6.678	0.978	34.23
	$^{214}\text{Pb}$	0.75	0.08	0.494	0.072	2.53
Thorium	$^{228}\text{Ac}$	0.49	0.18	1.134	0.166	5.81
	$^{208}\text{Tl}$	0.23	0.07	2.847	0.404	14.59
	$^{212}\text{Pb}$	0.30	0.04	0.094	0.013	0.48
	$^{212}\text{Bi}$	0.66	0.19	0.184	0.032	0.94
None	$^{40}\text{K}$	15.36	1.68	7.733	1.095	39.64
	$^{231}\text{Th}$	0.51	0.07	0.008	0.001	0.04
	X-rays			0.188	0.027	0.96
	Annihilation			0.083	0.012	0.42

In addition, the effective dose rate is about 3.5 times higher than in Modane (one of the main European ULs) [34]. These results show that a salt chamber in the Polkowice-Sieroszowice mine is a better place to establish a low-level underground laboratory. On the other hand, Lubin excavations can be used for other purposes where such low background radiation is not needed.

### 3.2. The Ratio of K-40/Bi-214

Similarly, as in our previous works [21,22,35,36], the ratio of  $^{40}\text{K}/^{214}\text{Bi}$  was determined. The ratio of the number of counts under the 1460.8 keV ( $^{40}\text{K}$ ) and 1764.5 keV ( $^{214}\text{Bi}$ ) lines helps to distinguish between shallow and deep underground locations.  $^{214}\text{Bi}$  isotope comes from the uranium series in the surrounding rock and also is derived from the radon, while  $^{40}\text{K}$  is incorporated in rocks only. In the investigated location, the  $^{40}\text{K}/^{214}\text{Bi}$  ratio is equal to 7.1, which points out that we are dealing with a deep location.

### 3.3. Radon Concentration in Air

The measurements were performed from 21 March to 23 March using a 2-day protocol. The concentration was in the range of 0 to  $15.3 \text{ Bq}/\text{m}^3$ , with the arithmetic mean equal to  $7.1 \pm 0.5 \text{ Bq}/\text{m}^3$  and the median equal to  $7.1 \text{ Bq}/\text{m}^3$ . Moreover, no significant changes in radon concentration in the air over measurement time were observed. The previous measurement of radon concentration in the air in the Polkowice-Sieroszowice mine, within the anhydrite layer, also showed very low values [21], with the median equal to  $4.8 \text{ Bq}/\text{m}^3$ . Exposure to high radon concentrations in the air can lead to lung cancer. Therefore, a limit on radon level in buildings intended for people and in workplaces has been introduced to be equal to  $300 \text{ Bq}/\text{m}^3$  [37–39]. The measured radon concentration in the air is significantly

lower than the established reference level. The comparison of underground laboratories in terms of radon concentration previously showed [40] that the main factors determining its concentration are: radionuclide concentration in the rock, ventilation, temperature, and humidity. Low concentrations of radionuclides, including radon, are crucial in research conducted by underground laboratories [41,42], and therefore special constructions are being developed dedicated to radon reduction [43,44].

### 3.4. Radioactivity Content in Water and Rocks Samples

The  $^{226}\text{Ra}$  activity concentrations in investigated rocks samples ranged from  $37.3 \pm 1.4$  Bq/kg to  $247 \pm 9$  Bq/kg (Table 2), with the mean equal to 109 Bq/kg and the median of 72 Bq/kg.  $^{228}\text{Ra}$  concentrations are in the range of  $16.1 \pm 0.4$ – $30.0 \pm 0.8$  Bq/kg, with the mean and the median equal to 17 Bq/kg and 20 Bq/kg, respectively. For the  $^{40}\text{K}$  isotope, the concentrations reached the value of  $927 \pm 15$  Bq/kg (mean: 669 Bq/kg, median: 613 Bq/kg). According to the literature data of the European Commission [45], the average worldwide  $^{226}\text{Ra}$ ,  $^{232}\text{Th}$ , and  $^{40}\text{K}$  concentrations in the earth's crust are equal to 40 Bq/kg, 40 Bq/kg and 400 Bq/kg, respectively. Analyzing the data provided in Table 2, the highest concentrations of the investigated isotopes are observed for shales. The lowest concentrations of  $^{226,228}\text{Ra}$  and  $^{40}\text{K}$  isotopes were observed in the sandstone samples. Moreover, sandstone and dolomite samples are characterized by similar concentrations of the  $^{228}\text{Ra}$  and  $^{40}\text{K}$  isotopes and different values of the  $^{226}\text{Ra}$  isotope concentrations (higher in the case of dolomite than in sandstone). The  $^{234,238}\text{U}$  concentrations ranged from  $43.4 \pm 4.6$  Bq/kg to  $247 \pm 18$  Bq/kg and from  $45.5 \pm 4.7$  Bq/kg to  $249 \pm 19$  Bq/kg, with the median equal to 72 Bq/kg and 74 Bq/kg, respectively. A previous study [21] of radionuclide content in anhydrite rocks in the Polkowice-Sieroszowice mine, at a depth of 1014.4 m, showed lower concentrations with the median equal to 1.1 Bq/kg, 0.2 Bq/kg and 8.9 Bq/kg for  $^{226}\text{Ra}$ ,  $^{228}\text{Ra}$  and  $^{40}\text{K}$ , respectively. The uranium content, calculated based on  $^{238}\text{U}$  concentration, is in the range of  $3.7 \pm 0.4$  mg/kg to  $20.2 \pm 1.5$  mg/kg. Additionally, a similar trend in the variability of the  $^{234,238}\text{U}$  concentrations in the analyzed samples was observed, as in the case of the  $^{226}\text{Ra}$  isotope. The previous studies of uranium content in copper ore deposits in the Fore-Sudetic Monocline in Poland showed values up to 163 ppm [46]. Sun Y-Z et al. [47] indicated that uranium accumulates in the Coppershale due to the redox boundary (due to the presence of organic matter) between the Coppershale and the Rotliegende. Uranium concentrations in the analyzed samples (Table 2) are 3 to 8 times higher than  $^{228}\text{Ra}$  and confirm previous studies [16,46]. Moreover, Piestrzyński [16] noted that thorium is present in the Coppershale in small amounts up to 5 ppm and observed a weak negative correlation ( $r = -0.25$ ) of thorium with uranium.

**Table 2.** Activity concentration of  $^{226}\text{Ra}$ ,  $^{228}\text{Ra}$ ,  $^{40}\text{K}$ ,  $^{238,234}\text{U}$ , uranium content,  $^{234}\text{U}/^{238}\text{U}$ , and  $^{226}\text{Ra}/^{238}\text{U}$  activity ratios in investigated rock samples.

Sample	$^{226}\text{Ra}$ [Bq/kg]	$^{228}\text{Ra}(^{228}\text{Ac})$ [Bq/kg]	$^{40}\text{K}$ [Bq/kg]	$^{238}\text{U}$ [Bq/kg]	$^{234}\text{U}$ [Bq/kg]	U [mg/kg]	$^{234}\text{U}/^{238}\text{U}$	$^{226}\text{Ra}/^{238}\text{U}$
sandstone	$40.1 \pm 1.5$	$16.5 \pm 0.5$	$586 \pm 10$	$58.1 \pm 3.2$	$58.2 \pm 3.2$	$4.7 \pm 0.3$	$1.0 \pm 0.1$	$0.7 \pm 0.1$
sandstone	$37.3 \pm 1.4$	$16.1 \pm 0.4$	$531 \pm 9$	$45.5 \pm 4.7$	$43.4 \pm 4.6$	$3.7 \pm 0.4$	$1.0 \pm 0.1$	$0.8 \pm 0.1$
dolomite	$65.9 \pm 2.4$	$17.2 \pm 0.4$	$641 \pm 10$	$61.6 \pm 4.5$	$55.5 \pm 4.1$	$5.0 \pm 0.4$	$0.9 \pm 0.1$	$1.1 \pm 0.1$
dolomite	$79.0 \pm 2.9$	$16.1 \pm 0.4$	$580 \pm 10$	$87.3 \pm 5.7$	$86.1 \pm 5.6$	$7.1 \pm 0.5$	$1.0 \pm 0.1$	$0.9 \pm 0.1$
shale	$186 \pm 7$	$21.5 \pm 0.5$	$747 \pm 12$	$129 \pm 8$	$124 \pm 7$	$10.5 \pm 0.6$	$1.0 \pm 0.1$	$1.4 \pm 0.1$
shale	$247 \pm 9$	$30.0 \pm 0.8$	$927 \pm 15$	$249 \pm 19$	$247 \pm 18$	$20.2 \pm 1.5$	$1.0 \pm 0.1$	$1.0 \pm 0.1$

The analysis of the  $^{234}\text{U}/^{238}\text{U}$  activity ratio for analyzed rock samples indicates a radioactivity equilibrium between these two isotopes. On the other hand, the  $^{226}\text{Ra}/^{238}\text{U}$  activity ratio varied from  $0.7 \pm 0.1$  to  $1.4 \pm 0.1$ , with the mean and median equal to 1.0 and 0.9, respectively. Slightly lower values of the  $^{226}\text{Ra}/^{238}\text{U}$  activity ratios were observed in the case of sandstones.

The concentration of  $^{234,238}\text{U}$  isotopes in the analyzed water sample was equal to  $220 \pm 15$  mBq/L and  $111 \pm 8$  mBq/L, respectively. The uranium content, calculated based on  $^{238}\text{U}$  concentration, was equal to  $9.0 \pm 0.7$   $\mu\text{g/L}$ . The occurrence of uranium in water results from leaching this element from the reservoir rocks, and the main factors determining the presence of uranium in waters are the content of radionuclides in rocks, reservoir rocks composition, pH, oxidation potential, mineral dissolution, partial pressure of  $\text{CO}_2$ , reservoir rocks composition [48]. The uranium  $^{234}\text{U}/^{238}\text{U}$  activity ratio was equal to  $2.0 \pm 0.2$ . This is due to the selective leaching of the  $^{234}\text{U}$  isotope from the reservoir rocks or the  $\alpha$ -recoil transfer of the  $^{234}\text{Th}$  isotope from the rock to water. The processes responsible for observed disequilibrium between  $^{234,238}\text{U}$  isotopes in waters are extensively discussed in the literature [49,50].

### 3.5. Qualitative Neutron Activation Analysis

Additionally, the neutron activation of three samples of the collected rocks (anhydrite, shale, and sandstone) from the investigated location was performed. These were the same samples that were tested for the concentrations of uranium, potassium, and radium radioisotopes described in Section 3.4.

Each sample was activated with a neutron flux from a source of californium ( $^{252}\text{Cf}$ ). The activation time was similar for all samples and was about 21 days. Immediately after the completion of neutron activation, each sample was placed on the HPGe detector in a lead–copper shield (described in Section 2.3). Then, the spectrum of gamma radiation was measured. First, short measurement time was applied to identify short-lived radioisotopes, and subsequently, long measurements were taken to identify long-lived radioisotopes formed in the  $(n,\gamma)$  reaction.

The following isotopes were identified for each analyzed rock sample:  $^{56}\text{Mn}$ ,  $^{24}\text{Na}$ , and  $^{42}\text{K}$ . The isotope of  $^{65}\text{Zn}$  was observed in the case of dolomite and shale. The presence of  $^{60}\text{Co}$  was confirmed in the analysis of shale and sandstone samples. In the case of sandstone, the following isotopes were additionally identified:  $^{82}\text{Br}$  and  $^{76}\text{As}$ . Meanwhile, in the shale sample, the  $^{76}\text{As}$ ,  $^{64}\text{Cu}$ ,  $^{110\text{m}}\text{Ag}$  and  $^{46}\text{Sc}$  isotopes were additionally observed.

Based on the analysis of neutron activation, it can be concluded that the radioisotopes were produced by the reaction  $(n,\gamma)$  with minerals of copper and other metals present in the tested samples. In this way, the resulting radioisotopes can increase radioactivity in the investigated location.

### 3.6. Neutron Flux Results

Data were collected over two days, in two series of 20 h. The average rate of neutron registration by a single counter was  $7.1 \pm 2.2$   $\text{h}^{-1}$  for Centronic counters and  $3.4 \pm 1.2$   $\text{h}^{-1}$  for ZDAJ counters, which corresponds well with the fact that the Centronic counter has twice the surface area than ZDAJ counter. The results for the individual counters are given in Table 3.

**Table 3.** The neutron counting rate per hour, for particular Centronic and ZDAJ counters.

Centronic	ZDAJ
$8.1 \pm 1.8$	$3.9 \pm 1.1$
$7.6 \pm 2.1$	$3.5 \pm 1.1$
$7.3 \pm 2.7$	$3.3 \pm 1.0$
$7.8 \pm 2.3$	$3.5 \pm 1.7$

After comparing the measured registration rate with the setup simulation, we obtain that the neutron flux is  $4.2 \pm 1.2 \times 10^{-6}$   $\text{cm}^{-2} \text{s}^{-1}$  for Centronic counters and  $4.1 \pm 1.5 \times 10^{-6}$   $\text{cm}^{-2} \text{s}^{-1}$  for ZDAJ counters. So, as the final result of the measurement, we will take their average:  $4.2 \pm 0.9 \times 10^{-6}$   $\text{cm}^{-2} \text{s}^{-1}$ .

This result, compared with the results of measurements carried out in other locations using a similar measurement set, is presented in Table 4 (extended version based on [22]).

**Table 4.** Comparison of thermal neutron flux measurement in different European underground locations.

Location	Flux of Thermal Neutrons ( $\times 10^{-6} \text{ cm}^{-2} \text{ s}^{-1}$ )
Lubin (Poland) (this work)	$4.2 \pm 0.9$
Polkowice-Sieroszowice (Poland)	$2.0 \pm 0.2$
Barbara (Poland)	$8.6 \pm 1.1$
Gran Sasso, (Italy)	$0.56 \pm 0.22$
Slanic Prahova, (Romania)	$0.12 \pm 0.05$
Freiberg, (Germany)	$3.12 \pm 0.10$
Pyhäsalmi; Lab2 (Finland)	$17.30 \pm 0.10$

The neutron flux in the Lubin mine is approximately twice as high as that obtained in Polkowice-Sieroszowice [21], even though the measurements were made using the same apparatus and in the same deposit. The most likely explanation for this difference is the different rock compositions in both locations. However, the different ventilation efficiency cannot be ignored in explaining the observed difference in the neutron flux.

### 3.7. Radiological Risk Assessment

Several risk indicators are used in the literature to estimate the potential radiation hazard from exposure to external gamma radiation emitted from building materials, rocks and soils [51,52]. Among them, the following risk indicators are often used: external hazard index ( $H_{\text{ex}}$ ), radium equivalent activity ( $Ra_{\text{eq}}$ ); these parameters can be calculated based on the equations [51,53]:

$$Ra_{\text{eq}} = {}^{226}\text{Ra} + 1.43{}^{232}\text{Th} + 0.077{}^{40}\text{K}. \quad (2)$$

$$H_{\text{ex}} = \frac{{}^{226}\text{Ra}}{370} + \frac{{}^{232}\text{Th}}{259} + \frac{{}^{40}\text{K}}{4810}. \quad (3)$$

where the activity concentration of  ${}^{226}\text{Ra}$ ,  ${}^{232}\text{Th}$ , and  ${}^{40}\text{K}$  isotopes are expressed in Bq/kg. In risk estimation, the  ${}^{228}\text{Ra}$  concentration was used to express  ${}^{232}\text{Th}$  activity. The calculated  $Ra_{\text{eq}}$  and  $H_{\text{ex}}$  values are presented in Table 5.

**Table 5.** Radium equivalent activity ( $Ra_{\text{eq}}$ ), external hazard index ( $H_{\text{ex}}$ ), absorbed dose rate (D) [nGy/h], and annual effective dose (ED) [mSv/y] estimated based on the  ${}^{226,228}\text{Ra}$  and  ${}^{40}\text{K}$  concentrations in collected rock samples.

Sample	$Ra_{\text{eq}}$ [Bq/kg]	$H_{\text{ex}}$	D [nGy/h]	ED [mSv/y]
sandstone	109	0.29	373	0.43
sandstone	101	0.27	339	0.39
dolomite	140	0.38	418	0.48
dolomite	147	0.40	387	0.45
shale	274	0.74	538	0.62
shale	362	0.98	675	0.78

The maximum allowed risk indicator should not exceed 370 Bq/kg and 1 for  $Ra_{\text{eq}}$  and  $H_{\text{ex}}$ , respectively, to keep the external gamma radiation dose below 1.5 mSv/y [51,53]. The highest  $Ra_{\text{eq}}$  and  $H_{\text{ex}}$  values were obtained for shale samples, which are close to established limits. The median values of  $Ra_{\text{eq}}$  and  $H_{\text{ex}}$  are equal to 143 Bq/kg and 0.39, respectively. It is worth emphasizing that the highest  ${}^{226,228}\text{Ra}$  and  ${}^{40}\text{K}$  concentrations and evaluated risk indicators were obtained for shales, which constitute a negligible fraction (about 1%) of the entire rocks present in the measurement location.

The absorbed dose rate (D) expressed in [nGy/h] can be calculated based on (Equation (4)) [51,54] and characterize the absorbed gamma dose rate in the air at a high of 1 m above the ground level from uniformly distributed  ${}^{226}\text{Ra}$ ,  ${}^{232}\text{Th}$ , and  ${}^{40}\text{K}$  radionuclides:

$$D \left[ \frac{\text{nGy}}{\text{h}} \right] = 0.462{}^{226}\text{Ra} + 0.604{}^{232}\text{Th} + 0.0417{}^{40}\text{K}. \quad (4)$$

The United Nations Scientific Committee on the Effects of Atomic Radiation [55] indicates that population-weighted and the median value of the absorbed dose rate in the air outdoor from terrestrial  $^{40}\text{K}$ ,  $^{226}\text{Ra}$ , and  $^{232}\text{Th}$  radionuclides in the soil is equal to 60 and 51 [nGy/h], respectively. However, the calculated values of absorbed dose rate (Table 5) are higher than the above-cited values in the range of values presented in the literature [56,57]. The values of the absorbed dose rate calculated based on laboratory measurements of rock samples are higher than the above-reported dose rate estimated based on the photon flux to dose conversion factors taken from the ICRP report [23].

Based on the absorbed dose rate (D), the annual effective dose rate (ED) in [mSv/y] can be calculated according to Equation (5):

$$\text{ED} \left[ \frac{\text{mSv}}{\text{y}} \right] = D \times 0.7 \times \text{OF} \times 10^{-6}. \quad (5)$$

where the occupancy factor was calculated as follows:

$$\text{OF} = \frac{7 \text{ h}}{\text{day}} \frac{5 \text{ days}}{\text{week}} \frac{47 \text{ weeks}}{\text{y}} = \frac{1645 \text{ h}}{\text{y}}. \quad (6)$$

According to the UNSCEAR report [55], the conversion coefficient from the absorbed dose in the air to the effective dose received by adults is equal to 0.7 [Sv/Gy]. In dose assessment, the daily seven-hour working time was assumed (staying in the place from which the samples were taken). The calculated effective radiation doses are presented in Table 5, and for the shale sample reaches the value of 0.78 mSv/y. The calculated weighted mean value of the effective radiation dose is equal to 0.44 mSv/y, which is significantly below the limit of 1 mSv/y [58]. It should be emphasized that the highest risk indicators were recorded for shale samples (Table 5), which constitute a negligible fraction (about 1%) of rocks.

### 3.8. Relation between Local Geology and Radiation Level

There are three main elements responsible for natural radiation in sedimentary basins: potassium, uranium and thorium. Potassium in sedimentary rocks is concentrated in sylvite, carnallite and polyhalite but can be found, in smaller amounts, in more common minerals such as some clays and feldspars. Uranium can be adsorbed onto organic matter or associated with phosphates. Thorium can be adsorbed onto terrestrial clays such as kaolinite [59].

The main uranium carrier in or close to ore-bearing horizons is secondary thucholite. As uranium probably was remobilized from thick red sandstones [60] by ascending brines, the biggest concentrations are recorded on or close to the Weissliegend and Copper-shale boundary [16,61]. Gamma radiation anomaly zones were identified in mining areas (Figure 1).

Locally, a “thucholitic shale”, up to 4 cm thick, with average U content of 180 ppm and Th of 30 ppm, was recognized by Kucha [61]. An average uranium content of 61.5 ppm and 5.1 ppm for thorium in Copper-shale, decreasing to avg. 10.6 ppm U and 0.9 ppm Th in Zechstein Limestone (Lubin-Sieroszowice district), were noted [16]. In general, fragments abundant with organic matter are enriched in uranium. Additionally, phosphates in shales also show significant amounts of U up to 0.24 wt.% [16].

Sylvite, carnallite, and polyhalite are minerals precipitated in the late stage of the evaporation cycle or diagenetic minerals connected to that deposition. They occur in Zechstein sediments in the described basin but not in the mining district area (at least not in significant volumes).

In good agreement with the described literature data of radiation distribution, in the described lithology profile, are natural gamma-ray logs. They provide information on combined K, U, and Th gamma radiation, or they measure specific wavelengths of gamma-ray output from radioactive elements stored in the rock formation. The measured natural

radioactivity of rocks is compared with that of a known standard rock and presented in [API] unit, defined by American Petroleum Institute [59].

Based on wire logs data reports made by Geofizyka Toruń and Geofizyka Kraków as part of the KGHM Polska Miedź S.A. exploration program (2015–2021)—north of the mining areas—radiation in lithological profiles can be described (Figure 6).

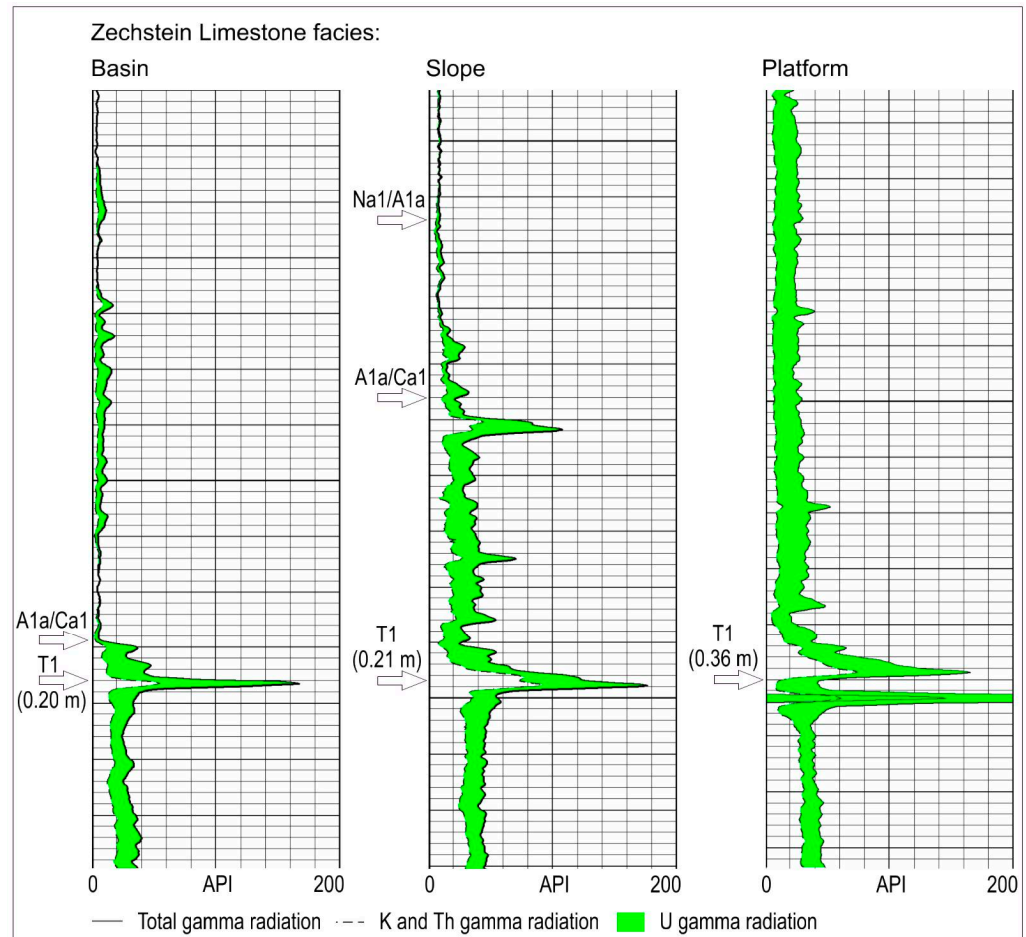


**Figure 6.** Examples of natural gamma radiation profiles: total, U, and K + Th, with lithostratigraphic boundaries (according to: [62–64]).

In general, according to gamma logs (Figure 6), a decrease in natural radiation values is observed from the upper parts of sandstones through carbonates to anhydrites and salts of the Werra cyclothem. If Coppershale occurs in the profile, the high gamma-ray response is observed within or at the base of the thin shale layer. In a few profiles from Zechstein Limestone platform facies, another intensive, occasionally the strongest, radioactivity is observed—2–8 m below the sandstone–shale boundary. In drillholes, from the basin and less often from slope facies, a much smaller anomaly close to the carbonate–anhydrite boundary can be observed.

If instead of a salt layer, anhydrite breccia was drilled, another peak could be observed, as this rock formation consists of an important admixture of clay minerals. In general, gamma logs provide information about layers with clay minerals or abundant in organic matter. In some cases, it can be related to secondary uranium concentrations.

#### 4. Conclusions

For years, attempts have been made to build an underground laboratory in Poland and to search for a convenient location. Therefore, a detailed characterization in terms of

the level of natural radioactivity of the underground location in the Lubin mine has been carried out.

The laboratory analysis showed the variability of  $^{234,238}\text{U}$ ,  $^{226,228}\text{Ra}$  and  $^{40}\text{K}$  concentrations in the analyzed rock samples, and the highest values were observed in the case of shales. Moreover, the concentrations of  $^{234,238}\text{U}$  and  $^{226}\text{Ra}$  isotopes were higher than  $^{228}\text{Ra}$ . The rock samples were characterized by higher concentrations of the analyzed radionuclides in relation to the rocks collected in the anhydrite layer (at a depth of 2941.8 m w.e.) and in the salt cavern (at a depth of 2700 m w.e.) in the Polkowice-Sieroszowice mine.

The concentration of radon in the air in the analyzed location was very low and comparable with the values obtained in the leading European laboratories. Moreover, the radon concentration was lower compared to the level in the salt cavern and comparable to the radon concentration measured in the anhydrite layer of the Polkowice-Sieroszowice mine.

Comparing the results obtained in the present study with the results of measurements in two other potential locations (the Polkowice-Sieroszowice mine anhydrite layer and salt chamber) of the underground laboratory (also owned by KGHM Polska Miedź S.A.), it can be concluded that the Lubin mine is characterized by a higher level of natural radioactivity than in the other locations which were under consideration. On the other hand, the analyzed location in the Lubin mine is characterized by several advantages related mostly to the safety of operation and easy access to the site. The development of an underground laboratory within the hard and stable stratum of dolomite and sandstone, with proper roof support, ensures the stability of the excavated chamber for dozen years. Another advantage of the potential location of UL in the Lubin mine is its close vicinity to one of the main ventilation shafts, significantly reducing the problem of high temperature and lack of efficient airflow. This fact also affects the possibility of transporting large components and parts of any detector. Moreover, a location at a depth of 2275 m w.e. ensures a significant reduction in muon flow. Unfortunately, up till now, the measurements of the muon flux have not been carried out. However, based on the literature data [65], the roughly estimated muon flux is about  $0.0014\text{ m}^{-2}\text{s}^{-1}$ .

**Author Contributions:** Conceptualization, A.W.-Ł., K.S., J.K., J.S. and K.P.-G.; methodology, A.W.-Ł., K.S., J.K., K.P.-G., K.J., J.S., M.K., J.O., P.T., W.M. and M.P.; formal analysis, A.W.-Ł., K.S. and K.J.; investigation, A.W.-Ł., K.S., J.K., K.P.-G., K.J., M.K., W.M. and M.P.; resources, L.S., T.S. and K.F.; writing—original draft preparation, A.W.-Ł., K.S., K.J., K.P.-G., L.S., T.S. and K.F.; writing—review and editing, A.W.-Ł., K.S., J.K., T.S. and K.F.; visualization, J.K., L.S., T.S. and K.F.; supervision, J.K. All authors have read and agreed to the published version of the manuscript.

**Funding:** This research was funded by: Research Excellence Initiative of the University of Silesia in Katowice.

**Data Availability Statement:** The data presented in this study are available on request from the corresponding author.

**Acknowledgments:** The authors would like to sincerely thank representatives of KGHM Polska Miedź S.A. for providing the necessary facilities and assistance during the field test.

**Conflicts of Interest:** The authors declare no conflict of interest.

## References

1. SKB. 2022. Available online: <https://www.skb.com/research-and-technology/laboratories/the-aspo-hard-rock-laboratory/> (accessed on 7 September 2022).
2. Zalewska, A.; Pytel, W.; Chorowski, M.; Cygan, S.; Hanzel, S.; Januszewska, K.; Jaroń, L.; Kisiel, J.; Lankof, L.; Markiewicz, A.; et al. Laguna in Polkowice–Sieroszowice Mine in Poland. *Acta Phys. Pol. B* **2010**, *41*, 1803–1820.
3. Kisiel, J.; Budzanowski, M.; Chorowski, M.; Cygan, S.; Dorda, J.; Hanzel, S.; Harańczyk, M.; Horoszczak, L.; Januszewska, K.; Jaroń, L.; et al. SUNLAB—The Project of a Polish Underground Laboratory. *AIP Conf. Proc.* **2010**, *1304*, 326–330.
4. Autiero, D.; Aysto, J.; Badertscher, A.; Bezrukov, L.; Bouchez, J.; Bueno, A.; Busto, J.; Campagne, J.-E.; Cavata, C.; Chaussard, L.; et al. Large underground, liquid based detectors for astro-particle physics in Europe: Scientific case and prospects. *J. Cosm. Astropart. Phys.* **2007**, *2007*, 011. [[CrossRef](#)]
5. Hryniewicz, A.; Broda, R.J. *Man and Ionizing Radiation*; Wydaw Naukowe PWN: Warsaw, Poland, 2001; ISBN 9788301134952. (In Polish)

6. Karnkowski, P.H. Origin and evolution of the Polish Rotliegend Basin. In *Polish Geological Institute Special Papers 3*; Polish Geological Institute: Warsaw, Poland, 1999.
7. Błaszczyk, J.K. Palaeomorphology of Weissliegendes top as the control on facies variability in ore-bearing series of Lubin copperfield, southwestern Poland. *Geol. Sudet.* **1981**, *16*, 195–217, (In Polish, with English summary).
8. Jerzykiewicz, T.; Kijewski, P.; Mroczkowski, J.; Teisseyre, A.K. Origin of the Weissliegendes deposits of the Fore-Sudetic Monocline. *Geol. Sudet.* **1976**, *11*, 57–97. (In Polish)
9. Nemec, W.; Porebski, S.J. Weissliegendes sandstones: A transition from fluvial-aeolian to shallow-marine sedimentation (Lower Permian of the Fore-Sudetic Monocline). 1. Sedimentary structures and textural differentiation. *Ann. Soc. Geol. Pol.* **1977**, *47*, 387–418.
10. Kaczmarek, W.; Wasilewska-Błaszczyk, M.; Dudek, M. The Impact of Lithological Variability of Reservoir Rocks on the Quality Parameters of the Cu-Ag Deposit, Lubin–Głogów Copper District (LGCD). *Biul. Państw. Inst. Geol.* **2018**, *472*, 105–120. [[CrossRef](#)]
11. Peryt, T.M.; Jasionowski, M.; Raczyński, P.; Chłódek, K. Demise of the Jabłonna Reef (Zechstein Limestone) and the Onset of Gypsum Deposition (Wuchiapingian, West Poland): Carbonate-to-Evaporite Transition in a Saline Giant. *J. Palaeogeogr.* **2020**, *9*, 18. [[CrossRef](#)]
12. Smith, D.B. Rapid Marine Transgressions and Regressions of the Upper Permian Zechstein Sea. *JGS* **1979**, *136*, 155–156. [[CrossRef](#)]
13. Glennie, K.W.; Buller, A.T. The Permian Weissliegend of NW Europe: The Partial Deformation of Aeolian Dune Sands Caused by the Zechstein Transgression. *Sediment. Geol.* **1983**, *35*, 43–81. [[CrossRef](#)]
14. Kucha, H. Geochemistry of the Kupferschiefer, Poland. *Geol. Rundsch.* **1990**, *79*, 387–399. [[CrossRef](#)]
15. Oszczepalski, S.; Rydzewski, A. Palaeogeography and Sedimentary Model of the Kupferschiefer in Poland. In *The Zechstein Facies in Europe*; Peryt, T.M., Ed.; Springer: Berlin/Heidelberg, Germany, 1987; Volume 10, pp. 189–205. ISBN 9783540177104.
16. Piestrzyński, A. Uranium and Thorium in the Kupferschiefer Formation, Lower Zechstein, Poland. *Mineral. Depos.* **1990**, *25*, 146–151. [[CrossRef](#)]
17. Kucha, H.; Przyłowicz, W. Noble Metals in Organic Matter and Clay-Organic Matrices, Kupferschiefer, Poland. *Econ. Geol.* **1999**, *94*, 1137–1162. [[CrossRef](#)]
18. Wagner, R. Sediment stratigraphy and development of the Zechstein Basin in the Polish Lowlands. *Państw. Inst. Geol.* **1994**, *146*, 1–71.
19. Salski, W. Rozwój tektoniczny obszaru miedzionośnego monokliny przedsudeckiej. Tectonic development of the copper-bearing area of the Fore-Sudetic Monocline. *Ann. Soc. Geol. Pol.* **1977**, *47*, 27–48. (In Polish)
20. Dumicz, M.; Don, J. Analiza strukturalna monokliny przedsudeckiej w rejonie Polkowic [Structural analysis of the Fore-Sudetic Homocline in vicinities of Polkowice]. *Acta Univ. Wratislav.* **1977**, *378*, 279–297. (In Polish). *Prace Geologiczno-Mineralogiczne.*
21. Szkliniarz, K.; Walencik-Łata, A.; Kisiel, J.; Polaczek-Grelík, K.; Jędrzejczak, K.; Kasztelan, M.; Szabelski, J.; Orzechowski, J.; Tokarski, P.; Marszał, W.; et al. Characteristics of Natural Background Radiation in the Polkowice-Sierszowice Mine, Poland. *Energies* **2021**, *14*, 4261. [[CrossRef](#)]
22. Walencik-Łata, A.; Szkliniarz, K.; Kisiel, J.; Polaczek-Grelík, K.; Jędrzejczak, K.; Kasztelan, M.; Szabelski, J.; Orzechowski, J.; Tokarski, P.; Marszał, W.; et al. Characteristics of Natural Background Radiation in the GIG Experimental Mine ‘Barbara’, Poland. *Energies* **2022**, *15*, 685. [[CrossRef](#)]
23. Petoussi-Henss, N.; Bolch, W.E.; Eckerman, K.F.; Endo, A.; Hertel, H.; Hunt, J.; Pelliccioni, M.; Schlattl, H.; Zankl, M. *Conversion Coefficients for Radiological Protection Quantities for External Radiation Exposures*; Publication 116; Ann. ICRP 40(2–5); ICRP: Stockholm, Sweden, 2010.
24. Suomela, J. *Method for Determination of U-Isotopes in Water*; Swedish Radiation Institute Document 0282-4434, No. 93-14; Swedish Radiation Institute: Stockholm, Sweden, 1993.
25. Sill, C.W. Precipitation of Actinides as Fluorides or Hydroxides for High-Resolution Alpha Spectrometry. *Nucl. Chem. Waste Manag.* **1987**, *7*, 201–215. [[CrossRef](#)]
26. Walencik-Łata, A.; Smółka-Danielowska, D. <sup>234</sup>U, <sup>238</sup>U, <sup>226</sup>Ra, <sup>228</sup>Ra and <sup>40</sup>K Concentrations in Feed Coal and Its Combustion Products during Technological Processes in the Upper Silesian Industrial Region, Poland. *Environ. Pollut.* **2020**, *267*, 115462. [[CrossRef](#)]
27. Walencik-Łata, A.; Kozłowska, B.; Przylibski, T.A. Hydrochemical Behaviour of Dissolved Uranium in Selected Groundwaters of the Kłodzko Valley (SW Poland) and Its Application Possibilities as an Environmental Tracer. *Chemosphere* **2021**, *267*, 128911. [[CrossRef](#)] [[PubMed](#)]
28. Agostinelli, S.; Allison, J.; Amako, K.; Apostolakis, J.; Araujo, H.; Arce, P.; Asai, M.; Axen, D.; Banerjee, S.; Barrand, G.; et al. Geant4—A Simulation Toolkit. *Nuclear Instruments and Methods in Physics Research Section A: Accelerators, Spectrometers, Detectors and Associated Equipment* **2003**, *506*, 250–303. [[CrossRef](#)]
29. Malczewski, D.; Kisiel, J.; Dorda, J. Gamma Background Measurements in the Laboratoire Souterrain de Modane. *J. Radioanal. Nucl. Chem.* **2012**, *292*, 751–756. [[CrossRef](#)]
30. Malczewski, D.; Kisiel, J.; Dorda, J. Gamma Background Measurements in the Boulby Underground Laboratory. *J. Radioanal. Nucl. Chem.* **2013**, *298*, 1483–1489. [[CrossRef](#)] [[PubMed](#)]
31. Malczewski, D.; Kisiel, J.; Dorda, J. Gamma Background Measurements in the Gran Sasso National Laboratory. *J. Radioanal. Nucl. Chem.* **2013**, *295*, 749–754. [[CrossRef](#)] [[PubMed](#)]

32. Polaczek-Grelak, K.; Kisiel, J.; Walencik-Łata, A.; Mietelski, J.W.; Janowski, P.; Harańczyk, M.; Jurkowski, J.; Zalewska, A.; Kobziński, J.; Markowski, P.; et al. Lead shielding efficiency from the gamma background measurements in the salt cavern of the Polkowice–Sieroszowice copper mine. *J. Radioanal. Nucl. Chem.* **2015**, *308*, 773–780. [[CrossRef](#)] [[PubMed](#)]
33. Kisiel, J.; Budzanowski, M.; Dorda, J.; Kozak, K.; Mazur, J.; Mietelski, J.W.; Puchalska, M.; Tomankiewicz, E.; Zalewska, A. Measurements of natural radioactivity in the salt cavern of the Polkowice-Sieroszowice copper mine. *Acta Phys. Pol. B* **2010**, *41*, 1813–1819.
34. Coccia, E. Underground laboratories: Cosmic silence, loud science. *J. Phys. Conf. Ser.* **2010**, *203*, 012023. [[CrossRef](#)]
35. Polaczek-Grelak, K.; Walencik-Łata, A.; Szkliniarz, K.; Kisiel, J.; Jedrzejczak, K.; Szabelski, J.; Mueller, T.; Schreiter, F.; Djakonow, A.; Lewandowski, R.; et al. Characterization of the Radiation Environment at TU Bergakademie in Freiberg, Saxony, Germany. *Nucl. Instrum. Methods Phys. Res. Sect. A Accel. Spectrometers Detect. Assoc. Equip.* **2019**, *946*, 162652. [[CrossRef](#)]
36. Polaczek-Grelak, K.; Walencik-Łata, A.; Szkliniarz, K.; Kisiel, J.; Jedrzejczak, K.; Szabelski, J.; Kasztelan, M.; Orzechowski, J.; Tokarski, P.; Marszał, W.; et al. Natural Background Radiation at Lab 2 of Callio Lab, Pyhäsalmi Mine in Finland. *Nucl. Instrum. Methods Phys. Res. Sect. A Accel. Spectrometers Detect. Assoc. Equip.* **2020**, *969*, 164015. [[CrossRef](#)]
37. Council Directive 2013/59/Euratom of 5 December 2013 Laying down Basic Safety Standards for Protection against the Dangers Arising from Exposure to Ionising Radiation, and Repealing Directives 89/618/Euratom, 90/641/Euratom, 96/29/Euratom, 97/43/Euratom and 2003/122/Euratom. Available online: <https://eur-lex.europa.eu/LexUriServ/LexUriServ.do?uri=OJ:L:2014:013:0001:0073:EN:PDF> (accessed on 8 November 2022).
38. Decree of the Polish Council of Ministers. Dz.U. 2001, No. 3, Poz. 18. 2001; (In Polish). Available online: <https://isap.sejm.gov.pl/isap.nsf/download.xsp/WDU20010030018/U/D20010018Lj.pdf> (accessed on 8 November 2022).
39. Decree of the Polish Ministry of Health. M.P. 2021 poz. 169. 22 January 2021; (In Polish). Available online: <https://isap.sejm.gov.pl/isap.nsf/download.xsp/WMP20210000169/O/M20210169.pdf> (accessed on 8 November 2022).
40. Liu, C.; Ma, H.; Zeng, Z.; Cheng, J.; Li, J.; Zhang, H. Measurements of Radon Concentrations Using CR-39 Detectors in China JinPing Underground Laboratory (2015–2016). *arXiv* **2018**, arXiv:1806.06567.
41. Zuzel, G. Experience of gas purification and radon control in BOREXINO. *AIP Conf. Proc.* **2018**, *1921*, 050001. [[CrossRef](#)]
42. Benato, G.; Biare, D.; Bucci, C.; Paolo, L.D.; Drobizhev, A.; Kadel, R.W.; Kolomensky, Y.G.; Schreiner, J.; Singh, V.; Sipla, T.; et al. Radon Mitigation during the Installation of the CUORE  $0\nu\beta\beta$  Decay Detector. *J. Inst.* **2018**, *13*, P01010. [[CrossRef](#)]
43. Štekl, I.; Hůlka, J.; Mamedov, F.; Fojtík, P.; Čermáková, E.; Jílek, K.; Havelka, M.; Hodák, R.; Hýža, M. Low Radon Cleanroom for Underground Laboratories. *Front. Public Health* **2021**, *8*, 589891. [[CrossRef](#)] [[PubMed](#)]
44. Udovičić, V.; Grabež, B.; Dragić, A.; Banjanac, R.; Joković, D.; Panić, B.; Joksimović, D.; Puzović, J.; Aničin, I. Radon Problem in an Underground Low-Level Laboratory. *Radiat. Meas.* **2009**, *44*, 1009–1012. [[CrossRef](#)]
45. European Commission, Directorate-General for Environment, Radiological Protection Principles Concerning the Natural Radioactivity of Building Materials, Publications Office. 2000. Available online: <https://op.europa.eu/en/publication-detail/-/publication/988f3243-5259-43a5-b621-fbff662deeb0/language-en> (accessed on 8 November 2022).
46. Piestrzyński, A. Uranium and thorium in copper ore deposits on the Fore-Sudetic Monocline (SW Poland). *Mineral. Pol.* **1989**, *20*, 41–56.
47. Sun, Y.-Z.; Jinxi, W.; Shifeng, L.; Kankun, J.; Mingyue, L. Mechanism of Uranium Accumulation in the Kupferschiefer from Poland and Germany. *Energy Explor. Exploit.* **2005**, *23*, 463–473. [[CrossRef](#)]
48. Paces, J.B.; Ludwig, K.R.; Peterman, Z.E.; Neymark, L.A. 234U/238U Evidence for Local Recharge and Patterns of Ground-Water Flow in the Vicinity of Yucca Mountain, Nevada, USA. *Appl. Geochem.* **2002**, *17*, 751–779. [[CrossRef](#)]
49. Osmond, J.K.; Cowart, J.B. U-series nuclides as tracers in groundwater hydrology. In *Environmental Tracers in Subsurface Hydrogeology*; Cook, P.G., Herczeg, A.L., Eds.; Kluwer Academic Publishers: New York, NY, USA, 2000.
50. Suksi, J. Natural Uranium as a Tracer in Radionuclide Geosphere Transport Studies. Ph.D. Thesis, University of Helsinki, Helsinki, Finland, 2001. Available online: <https://urn.fi/URN:ISBN:952-10-0222-0> (accessed on 8 November 2022).
51. Jasaitis, D.; Pečiulienė, M. Natural Radioactivity and Radon Exhalation from Building Materials in Underground Parking Lots. *Appl. Sci.* **2021**, *11*, 7475. [[CrossRef](#)]
52. Medhat, M.E. Assessment of Radiation Hazards Due to Natural Radioactivity in Some Building Materials Used in Egyptian Dwellings. *Radiat. Prot. Dosim.* **2009**, *133*, 177–185. [[CrossRef](#)]
53. Lu, X.; Li, L.Y.; Wang, F.; Wang, L.; Zhang, X. Radiological Hazards of Coal and Ash Samples Collected from Xi’an Coal-Fired Power Plants of China. *Environ. Earth Sci.* **2012**, *66*, 1925–1932. [[CrossRef](#)]
54. Nwankwo, C.U.; Ogundare, F.O.; Folley, D.E. Radioactivity Concentration Variation with Depth and Assessment of Workers’ Doses in Selected Mining Sites. *J. Radiat. Res. Appl. Sci.* **2015**, *8*, 216–220. [[CrossRef](#)]
55. United Nations Scientific Committee on the Effects of Atomic Radiation (UNSCEAR). *Sources and Effects of Ionizing Radiation: Sources*; United Nations Publications: New York, NY, USA, 2000.
56. Inoue, K.; Fukushi, M.; Van Le, T.; Tsuruoka, H.; Kasahara, S.; Nimelan, V. Distribution of Gamma Radiation Dose Rate Related with Natural Radionuclides in All of Vietnam and Radiological Risk Assessment of the Built-up Environment. *Sci. Rep.* **2020**, *10*, 12428. [[CrossRef](#)]
57. Tzortzis, M.; Tsertos, H.; Christofides, S.; Christodoulides, G. Gamma Radiation Measurements and Dose Rates in Commercially-Used Natural Tiling Rocks (Granites). *J. Environ. Radioact.* **2003**, *70*, 223–235. [[CrossRef](#)]

58. The 2007 Recommendations of the International Commission on Radiological Protection. ICRP Publication 103. *Ann. ICRP* **2007**, *37*, 1–332. [[CrossRef](#)]
59. Gluyas, J.; Swarbrick, R. *Petroleum Geoscience*; Blackwell Publishing: Hoboken, NJ, USA, 2004; ISBN 0632037679.
60. Zielinski, R.A.; Bloch, S.; Walker, T.R. The Mobility and Distribution of Heavy Metals during the Formation of First Cycle Red Beds. *Econ. Geol.* **1983**, *78*, 1574–1589. [[CrossRef](#)]
61. Kucha, H. Platinum-Group Metals in the Zechstein Copper Deposits, Poland. *Econ. Geol.* **1982**, *77*, 1578–1591. [[CrossRef](#)]
62. Baudzis, A.; Marzec, D. Report on lithological wire logs data. Geofizyka Toruń: Toruń, Poland, 2019; (*unpublished work*).
63. Baudzis, A.; Marzec, D. Report A on lithological wire logs data. Geofizyka Toruń: Toruń, Poland, 2020; (*unpublished work*).
64. Baudzis, A.; Marzec, D. Report B on lithological wire logs data. Geofizyka Toruń: Toruń, Poland, 2020; (*unpublished work*).
65. Enqvist, T.; Mattila, A.; Föhr, V.; Jämsén, T.; Lehtola, M.; Narkilahti, J.; Joutsenvaara, J.; Nurmenniemi, S.; Peltoniemi, J.; Remes, H.; et al. Measurements of Muon Flux in the Pyhäsalmi Underground Laboratory. *Nucl. Instrum. Methods Phys. Res. Sect. A Accel. Spectrometers Detect. Assoc. Equip.* **2005**, *554*, 286–290. [[CrossRef](#)]